Energy management optimization of a gravitational energy harvester powering wireless sensor nodes for freight trains monitoring

Sustainable Energy Technologies and Assessments 70 (2024) 103964

Contents lists available at ScienceDirect

Sustainable Energy Technologies and Assessments

journal homepage: www.elsevier.com/locate/seta

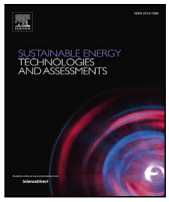

Energy management optimization of a gravitational energy harvester powering wireless sensor nodes for freight trains monitoring

Mirco Lo Monaco *, Caterina Russo, Aurelio Somà

Department of Mechanical and Aerospace Engineering, Politecnico di Torino, Corso Duca degli Abruzzi 24, Torino, 10129, Italy

ARTICLE INFO

Keywords:
Energy harvester
Wireless sensor network
Internet of things
Railways monitoring
Power management system

ABSTRACT

Energy harvesting is a promising solution for the realization of self-powered wireless sensor nodes (WSNs), minimizing battery waste and environmental impact. The harvesting devices studied in this paper are gravitational vibration-based energy harvesters (GVEHs), converting the ultra-low-frequency ambient vibrations of structures or vehicles into electric power. The main efficiency losses are related to the AC/DC rectification and battery storage processes. Experimental tests confirm the optimized layout of negative voltage converter (NVC) using MOSFETs and a schottky diode with a 1000 μF smoothing capacitor, achieving power rectification efficiency of 65%. The rectified and smoothed power is stored in a Li-Ion 3.6 V 40 mAh coin cell and supplied to the load, consisting of a 3.3 V micro-controller unit, temperature sensor and sub-GHz wireless communication module. A nano power boost charger with buck converter manages power between the battery and the load. Experimental battery charge tests are performed for charging power evaluation at different external excitation amplitudes and frequencies. WSN average power consumption is analyzed with master–slave communication tests at different signal strengths and relative distances between the nodes. Finally, a duty cycle between active and sleep phase is defined to guarantee continuous activity of the WSN and net positive charge to the battery.

Introduction

Energy harvesters (EHs) are renewable energy generators that can harness various ambient energy sources to generate an amount of power ranging from micro-Watts up to Watts, depending on the harvesting technique, conversion methodology and size [1]. These generators can be a suitable power supply for Internet of Things (IoT) devices. A major challenge hindering the full realization of IoT's potential lies in providing sufficient energy to devices in a self-sustaining manner. Due to factors like cost, convenience, and deployment in remote locations, most devices rely on batteries. As IoT market is forecasted to grow from 17 billion nodes in 2024 to 29 billion nodes in 2030 [2], the large-scale extensive use of batteries carries significant environmental consequences. The recent advancements in energy harvesting and storage technologies can address the aforementioned issue. The application of energy harvesters in the context of wireless sensor networks (WSNs) for remote monitoring is of great interest for scientific research [3]. WSNs powered by energy harvesters (EH-WSNs) with super-capacitors or rechargeable batteries are fully autonomous systems, having ideally infinite lifespan, requiring minimum maintenance and reducing environmental impact. The application fields of EH-WSN range from wearable devices [4,5] to smart homes and agriculture using photovoltaic cells [6,7] as well as industrial [8,9]. Other applications exploit wind energy [10,11] or ocean wave motion [12,13] for structural monitoring applications. Transportations field applications are also relevant [14,15], where vibrational energy harvesters (VEHs) are the most suited solutions [16]. Our research group has been studying energy harvesting solutions for monitoring applications in industrial vehicles and trains for several years [17,18].

VEHs exploit different conversion methodologies such as piezoelectric materials [19,20], electromagnetic induction [21–23], triboelectric effect [24] and hybrid configurations [25–27]. Our GVEHs belong to the electromagnetic energy harvester (EMEH) category, inducing voltage due to the relative motion of a permanent magnet respect to a coil [28]. An interesting application branch is the use of VEH-WSN for remote monitoring of railroads, both onboard and at tracks level [29,30]. These self-powered devices are implemented on trains or tracks and use RF or GSM communication for structural monitoring of vital parameters [31–33]. Researchers are focusing on the implementation of EMEHs onboard of freight wagons, since the supply of electricity is not guaranteed as opposed to passenger trains [34,35]. Wu et al. [36] propose a self-powered energy harvester exploiting trackside vertical vibrations to power a wireless sensor node. The device conversion efficiency achieves the value of 48.3% with an output power of 0.928 W. Liu et al. [37] propose a novel seesaw-inspired bistable energy

* Corresponding author.
E-mail addresses: mirco.lomonaco@polito.it (M. Lo Monaco), caterina.russo@polito.it (C. Russo), aurelio.soma@polito.it (A. Somà).

https://doi.org/10.1016/j.seta.2024.103964
Received 20 May 2024; Received in revised form 14 August 2024; Accepted 8 September 2024
Available online 13 September 2024

harvester for self-powered rail train condition monitoring, having a bandwidth of 18–39 Hz and generating a maximum value of 7.4 mW at 39 Hz and 6 g excitation. Gao et al. [38] propose a energy harvester capable of collecting vibration energy in both lateral and vertical directions. The energy conversion circuit has a conversion efficiency ranging from 40% to 65%, being able to supply power to an integrated pressure sensor unit.

The GVEH presented in this paper is destined to scavenge ultra-low frequency vibrations of freight trains to supply power to a WSN for remote monitoring. The AC/DC rectification circuit must be carefully designed to maximize conversion efficiency and provide a sufficient charge to the battery powering the WSN. Researchers have carried out optimization studies on different rectification architectures for low-power energy harvesters, using passive [39–44] or active components [45–47]. However, these works lack of actual correlation between the real working conditions of the harvester and the management circuit efficiency. This paper aims at giving a novel design approach of the power management system by evaluating the rectification and storage efficiencies related to the resonance conditions of the GVEH. As a result, the rectification efficiency Frequency Response Functions in terms of RMS power are integrated respect to the vibration frequencies to compute a single index value, considering the high variability of the ambient input on the freight train. Moreover, the smoothing capacitor should be optimized performing a trade-off between DC voltage mean value and ripple. Battery charge tests at GVEH resonance frequencies are performed for charge time estimation. Finally, the node power draw is analyzed, comparing RX-TX consumption at different signal strengths of the RF communication module. A duty cycle between sleep and active phases of the node is defined for different GVEH working conditions, ideally guaranteeing long-lasting performance [48,49].

This paper is structured as follows: Section "Materials and Methods" regards the overview and working principle of the GVEH, the description of the WSN components and the experimental setup for the laboratory tests. Section "Results" shows the experimental results of the optimization analysis of the AC/DC rectification circuit, battery charge tests, master–slave RF communication tests at different signal strengths and relative distances. At last, the WSN duty cycle is defined according to the GVEH generated power under different excitations. Section "Conclusions" discusses the above-mentioned results and draws final conclusions.

Materials and methods

This section regards a detailed description of the EH-WSN system. Firstly, in Section "Gravitational Energy Harvester overview" the GVEH architecture and main characteristics are outlined. Secondly, the WSN components and respective functions are defined in Section "Wireless sensor node description". Finally, Section "Experimental setup" reports the experimental setup for the dynamic laboratory tests.

Gravitational energy harvester overview

A gravitational vibration-based energy harvester (or GVEH) is a subcategory of electromagnetic energy harvesters exploiting the variation of a permanent magnet magnetic flux due to its relative motion respect to a coil under an external excitation, according to Faraday–Lenz law. The main components of a VEH are a permanent magnet (proof mass), spring (traditional helicoidal or different types) and coils. VEHs can be modeled as simple one-degree-of-freedom mass–spring–damper systems [28]. Numerous related research regard VEH using mechanical helicoidal springs [50,51] or innovative designs [52]. The peculiarity of a GVEH is the use of a magnetic spring that suspends the permanent magnet thanks to a repulsive force arising from its interaction with another permanent magnet [53–55]. The latter is fixed at the bottom end of a tube inside which the permanent magnet oscillates. The absence of another fixed magnet at the top end of the tube results in an asymmetric non-linear spring having softening behavior. This characteristic shows four advantages for the EH-WSN destined application. Firstly, magnetic springs have low natural frequencies compatible with the fundamental frequencies of the vibrating structures/vehicles, maximizing the power generation (2–10 Hz for freight wagons) [34,38,56,57]. Secondly, the spring non-linearity leads to the broadening of the generator frequency response and thus increases the conversion efficiency of the ambient vibrations [58]. Moreover, the softening behavior is characterized by the reduction of the GVEH natural frequency with increasing excitation, further increasing the system suitability for the destined application [53,54]. Finally, the absence of mechanical components increases the system durability [55]. The GVEH damping characteristic results from the combination of a viscous-type component related to air friction and a non-linear electromagnetic component related to the induction of parasitic currents inside the coils [53]. The pick-up coils are wrapped around the outer diameter of the tube, having height, number of turns, cross-section diameter and location along the tube length carefully designed for maximization of generated power. The GVEH used for the EH-WSN system is the result of a detailed numerical and experimentally-validated design procedure that starts from the dimensions of the two permanent magnets forming the spring [53]. The magnets size influences the GVEH natural frequencies, the moving magnet equilibrium position, the power generation and the coil optimum number of turns, axial length and location. Supplementary material includes representation of the GVEH highlighting its components, main characteristics and their respective values.

Wireless sensor node description

EH-WSN systems are energetically and operatively autonomous, thus being able to provide long-lasting reliable data with minimum maintenance and in harsh environments overcoming installation constraints [3,59]. The GVEH generates AC power that must be correctly managed to be effectively supplied to the WSN. Hence, the WSN design involves the implementation of specific components and circuitry as follows.

1. AC/DC Rectification Circuit (ADRC)
2. Smoothing Capacitor (SC)
3. Battery charging module (BCM)
4. Buck–boost DC–DC converter (BBDC)
5. Storage Unit (STU)
6. Micro-controller Unit (MCU)
7. Sensor Unit (SU)
8. Communication Unit (CU)

The ADRC uses four MOSFETs (two PFETs and two NFETs) in a negative voltage converter configuration and a schottky diode to block reverse current flow from the electrolytic smoothing capacitor of 1000 uF. This configuration is the result of a rectification efficiency optimization procedure that is accurately described is Section "AC/DC rectification circuit optimization". DC power can be used to power the load (MCU, SU and CM) and charge a STU. Therefore, the Texas Instruments BQ25570 power management integrated circuit (PMIC) is introduced, featuring both boosted BCM and BBDC. This device is specifically designed for energy harvesting applications, being able to efficiently extract microwatts to milliwatts. The battery management features ensure overcharge/discharge protection and voltage boost to a rechargeable battery. Moreover, the BQ25570 integrates a highly efficient, nano-power buck converter for providing a second power rail to the load with 3.3 V fixed voltage output [60]. STU is a rechargeable Li-Ion 3.6 V 40 mAh coin cell. MCU is an Arduino Pro Mini 3.3 V (Arduino srl, Italy) having ultra-low power consumption both in active and sleep modes, acting as a control unit for both SU and CU. SU is a MCP9808 temperature sensor breakout board (Microchip, 200 μA operating current) [61]. CU is a Sub-GHz RFM69HCW transceiver

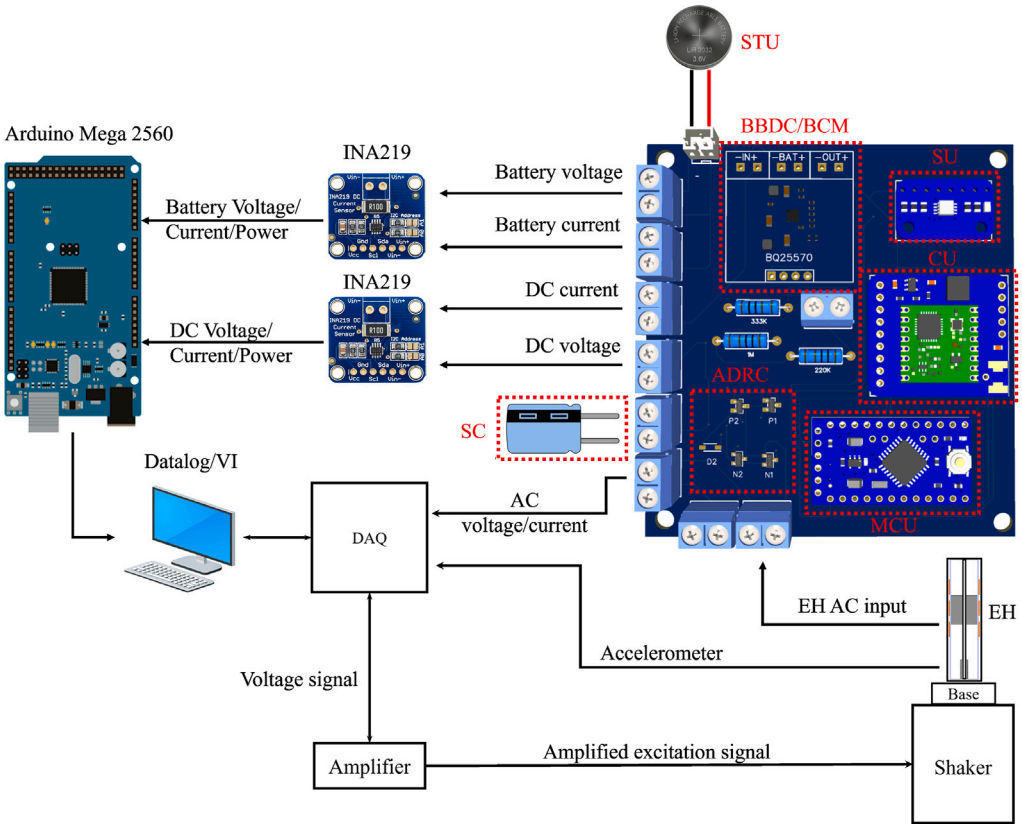

Fig. 1. Experimental setup scheme.

module operating in the license-free ISM (Industry Scientific and Medical) frequency bands [62]. Sub-GHz signals can propagate better with reduced blocking effects due to their long wavelengths, with extended communication range and low power consumption, thus implementing a solid communication solution for WSN applications [63]. Moreover, their low frequencies show the best potential also in metallic environments, such as industrial vehicles or freight trains, since the free-space path loss is directly proportional to the signal frequency [59]. Supplementary material includes a schematic representation of the EH-WSN circuit and components.

Experimental setup

Experimental tests giving the results reported in Section "Results" are performed on a laboratory testing workbench, which is schematized in Fig. 1. The EH generator is placed on a vibration exciter (TIRAvib 52110) operated by an analog power amplifier (TIRA BAA120) having variable gain control (TIRA GmbH, Schalkau, Germany). LabView (National Instruments, Austin, TX, USA) on a DAQ system supplies a pre-set sinusoidal voltage signal to the moving base of the shaker to excite the EH on a controlled acceleration amplitude and frequency. A IMI 608A11 piezoelectric accelerometer provides the closed-loop feedback signal (PCB Piezotronics, Depew, NY, USA). The DAQ allows to measure and visualize the AC voltage, current and power signals generated by the EH. This generated power is also fed into the WSN printed circuit board (PCB) designed by the authors. The DC rectified voltage signal after the ADRC and the charging voltage to the battery after the BCM/BBDC are measured and connected to a INA219 breakout board each (Adafruit Industries LLC, NY, USA) for current/power monitoring. The resulting values of voltage, current and power for the two DC and battery lines are stored on a datalogger controlled by an Arduino Mega (Arduino srl, Italy) for the rectification and storage efficiency evaluation.

Results

AC/DC rectification circuit optimization

Four full-wave passive AC/DC rectification circuits are tested:

1. Schottky diode bridge rectifier (SDBR)
2. Gate cross-coupled rectifier (GCCR)
3. Negative voltage converter (NVC)
4. Negative voltage converter with schottky diode (NVCd)

These configurations are the most commonly studied passive rectifiers for low-power applications as energy harvesting [40,64–66]. The rectification efficiency index is evaluated as the ratio between output DC voltage, measured by INA219 sensor, and input AC voltage for each ADRC. SDBR configuration uses a component having four schottky diodes (D4SBS4-7000, Shindengen, forward voltage drop = 550 mV) to rectify the full wave of the signal. GCCR and NVC both use four MOSFETs, two P-FETs (DMG2301LK-7, Diodes Incorporated, gate–source voltage threshold = 300 mV) and two N-FETs (DMG2302UK-7, Diodes Incorporated, gate–source voltage threshold = 300 mV), but their terminals have different connections in the respective configuration. The main losses in the voltage rectification process are due to the forward voltage drop in schottky diodes and gate–source voltage threshold in MOSFETs. Hence, the choice of the components is aimed at minimizing these variables to improve the efficiency. The rectified output is connected to a resistor (R_{load}) and the smoothing capacitor (SC). NVC configuration is tested with and without a schottky diode (NVCd) on the positive DC branch blocking reverse current flows that may occur when the output is not a pure resistive load. When SC is also connected, if the output voltage is greater than the input voltage, the MOSFETs allow bidirectional current flow, drastically reducing the efficiency [40]. Supplementary material includes the circuit diagrams

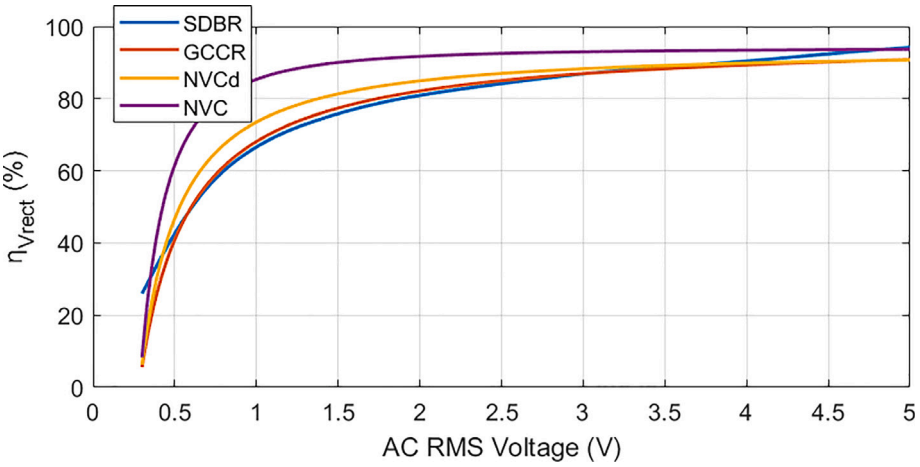

Fig. 2. Voltage rectification efficiency curves with pure resistive load of 600 Ω.

of the four tested ADRC configurations, where D, P, N are respectively schottky diodes, PFETs, NFETs.

For the first set of tests, the three ADRCs are connected to a pure resistive load of 600 Ω, being the optimum value evaluated through AC load tests reported in Fig. 5. Fig. 2 shows the fitted experimental voltage rectification efficiency curves with different input AC voltages for all the configurations. Voltage rectification efficiency (η_{Vrect}) is defined as the ratio between mean output DC voltage and input RMS AC voltage.

$$\eta_{Vrect} = \frac{V_{DC,mean}}{V_{AC,RMS}} \tag{1}$$

NVC has the best performance among all the other configurations, reaching almost 90% of efficiency already at low voltages around 1 V. The addition of the schottky diode to the NVC configuration (NVCd) slightly reduces the efficiency, but still outperforming GCCR and SDBR at almost every input voltages. GCCR and SDBR have close-to-identical efficiency curves. However, SDBR shows higher efficiency than GCCR and NVCd for high voltages.

Thereupon, the ADRCs are tested connecting the smoothing capacitor SC at the rectified DC output. Frequency Response Functions (FRFs) curves are derived by sweeping the excitation input frequencies from 3 to 10 Hz, with a fixed step of 0.1 Hz between 4 and 4.5 Hz for a greater resolution around the resonance frequency and a step of 0.5 Hz for the remaining values in the range, keeping the amplitude fixed at 0.4 g, and changing different SC sizes. FRFs are evaluated using NVCd configuration, which overall showed the most adequate performance with the pure resistive load, excluding the NVC since the connection of a reactive load strongly worsens the efficiency. R_{load} is kept constant at 600 Ω, being the power optimum value derived from load tests in AC conditions reported in Fig. 5. SC is necessary to reduce the ripple of the rectified voltage signal. Hence, DC voltage and power signals are considered in terms of both mean values and ripple values. Fig. 3 reports the mean DC power FRFs ($P_{DC,mean}$) in the first plot and the ratio between DC voltage ripple and mean values ($\eta_{Vripple}$) at different excitation frequencies in the second plot, connecting different SC sizes.

$$\eta_{Vripple} = \frac{V_{DC,ripple}}{V_{DC,mean}} \tag{2}$$

As can be seen in the first plot, the presence of SC highly dampens the resonance peak to a value of about 40%–50% respect to the peak without SC, worsening the performance with increasing capacities. Outside of the resonance frequency range of 3.8–5.2 Hz, SC size has a negligible effect on the mean generated power. However, as can be seen on the second plot, the absence of SC produces a voltage ripple of around 200% of the mean DC voltage value, resulting in high magnitude pulses that can be dangerous to the circuit. Increasing SC sizes leads to the reduction of $\eta_{Vripple}$ up to 1% for a capacity of 2200 μF. As a result, the choice of the SC size is a trade-off between ripple minimization and mean power reduction. The optimum SC has a capacity of 1000 μF, guaranteeing a voltage ripple less than 10% of mean voltage value at all excitation frequencies and leading to a maximum power reduction of 45% at resonance frequency.

Subsequently, all the ADRC configurations with the chosen SC are compared in terms of $\eta_{Vripple}$ and power efficiency ($\eta_{P,SC}$) defined as the ratio between DC mean power with SC (P_{SC}) respect to the mean power value without SC (P_{noSC}) at different excitation frequencies and amplitude of 0.4 g.

$$\eta_{P,SC} = \frac{P_{SC}}{P_{noSC}} \tag{3}$$

As can be seen in Fig. 4, NVC configuration has a considerable drop in efficiency when SC is connected, being a reactive load, resulting in an almost 90% power reduction in the resonance frequency range. NVC shows also the highest voltage ripple to mean value ratio, with a peak of about 20% at the resonance frequency. GCCR and SDBR configurations have almost identical and adequate behaviors at all frequencies for both studied variables. NVCd has the overall most satisfactory performance, following the same trend of GCCR and SDBR but with improvements outside the resonance frequency ranges. This can be related to the rectification efficiency curve reported in Fig. 2, where NVCd has greater performance at lower AC voltage than GCCR and SDBR. EH generates lower AC voltage when outside the resonance frequency following its Frequency Response Function (FRF), so a direct relation between the rectification efficiency and the working condition of the harvester can be derived. Hence, NVCd configuration is validated as the optimized ADRC, considering the EH FRF, and is chosen for the realization of the WSN circuit.

Figs. 3–4 show that the introduction of the SC dramatically reduces the output power in the resonance frequency range. All these curves are obtained connecting a resistive load having the optimum value of 600 Ω derived by GVEH load tests in AC. The dampening effect of SC may be related to the shifting of R_{load} optimum value. Fig. 5 reports the comparison between AC and DC load tests in terms of RMS load voltage, current and power. DC tests are performed with NVCd rectification circuit and optimum SC = 1000 μF. Both AC and DC curves are obtained in resonance conditions imposing an external excitation of 0.4 g amplitude at 4 Hz frequency. AC curves are more sensitive to the resistance variation than the DC curves. AC power curve has a peak of 32 mW at 600 Ω, maintaining high power values around 30 mW in a small range between 500–1200 Ω, but rapidly decreasing for higher resistances. The DC load voltage, current and power curves have lower values than the AC ones for R_{load} less than 1800 Ω. Nonetheless, DC

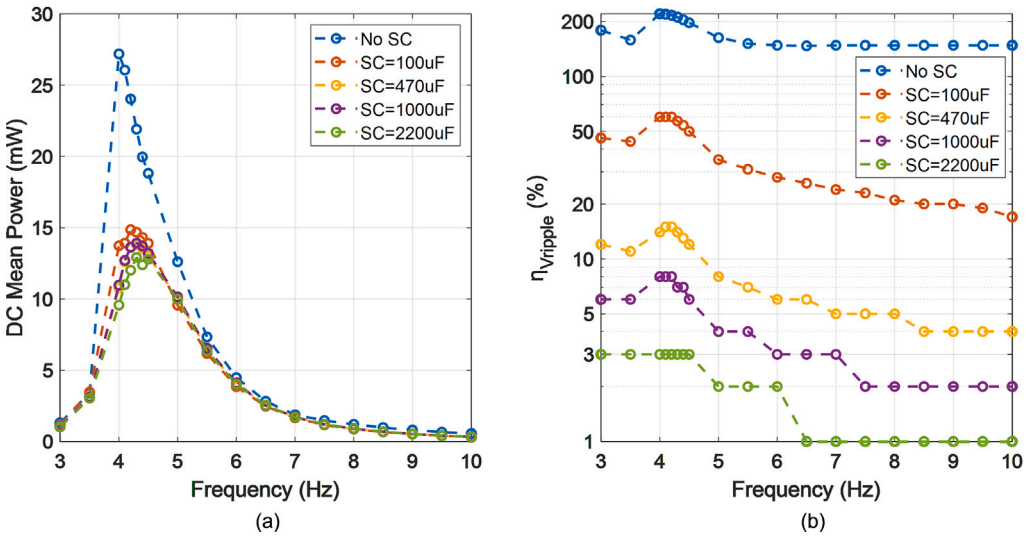

Fig. 3. Smoothing capacitor size effects on (a) DC mean power FRFs and (b) voltage ripple with R_{load} = 600 Ω and excitation amplitude 0.4 g.

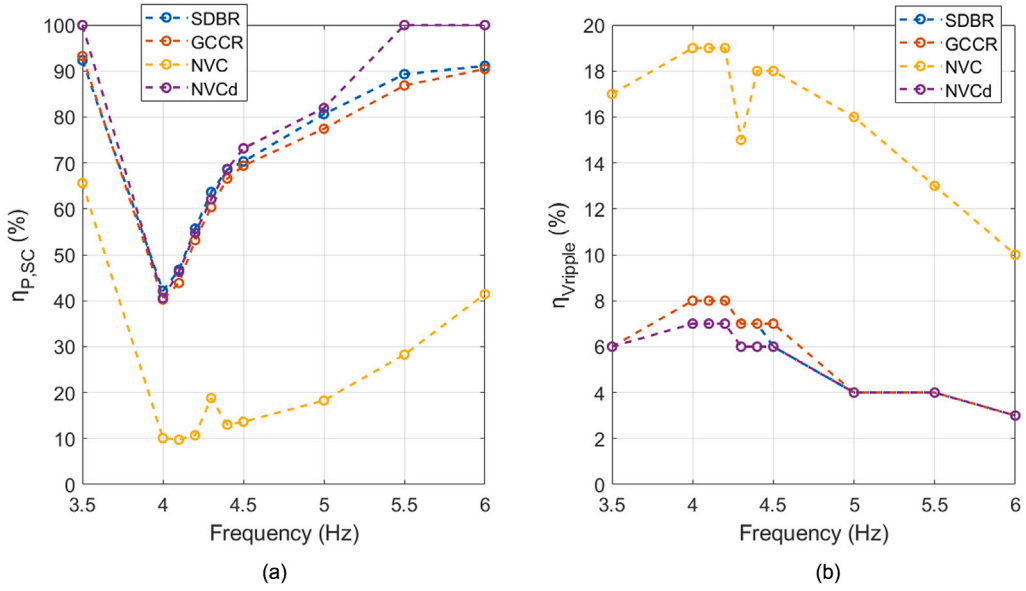

Fig. 4. ADRCs effect on (a) Mean DC power FRFs and (b) voltage ripple with R_{load} = 600 Ω, excitation amplitude 0.4 g and SC = μF.

power curve present a plateau-like behavior, maintaining an almost constant maximum value of about 20 mW for a wide range of R_{load} from 1000 to 4500 Ω, which is greater than the AC power starting from R_{load} values of 1800 Ω. As a result, the optimum resistance shifts from 600 Ω in AC to 1800 Ω in DC, increasing the maximum power generation of 57%. The smoothing capacitor size of 1000 μF is still optimized for the new resistive value, being the voltage ripple low level a key constraint in the circuit and the influence on the extracted power relatively limited as can be seen in Fig. 3.

Finally, AC and DC FRFs in optimized power configurations are compared to evaluate the overall efficiency of the proposed circuit and electronic components. More specifically, AC FRFs are computed connecting R_{load} = 600 Ω, while DC FRFs using NVCd, SC = 1000 μF and R_{load} = 1800 Ω. The excitation input ranges from 0.2 to 0.5 g with a frequency sweep from 3 to 7 Hz. Considering the rectification efficiency dependence on input AC voltage, it should not be computed for a specific excitation amplitude and frequency only, given the non-linear response of the GVEH. The proposed rectification efficiency index ($\eta_{Prect,int}$)is based on the ratio between the integral of the AC and DC FRF power curves.

$$\eta_{Prect,int} = \frac{\int_{fl}^{fu} P_{DC}\, df}{\int_{fl}^{fu} P_{RMS,AC}\, df} \tag{4}$$

Where fl and fu are respectively lower and upper frequency of the considered interval in Hz. This index allows to define an averaged performance of the ADRC normalized respect to the GVEH frequency response. As can be seen in Fig. 6 showing the comparison between AC and DC RMS power FRFs, $\eta_{Prect,int}$ is about 65% for 0.2–0.5 g excitation amplitudes and 3–7 Hz frequencies, which is a noticeably strong result considering the ultra-low-power applications.

Battery charge tests

The subsequent design phase of the EH-WSN system regards the optimization of the storage management. The use of a battery rather than a supercapacitor is a design choice related to the destined application of the device. Since the freight train motion is the energy source of the system, it is mandatory to guarantee continuative power to the

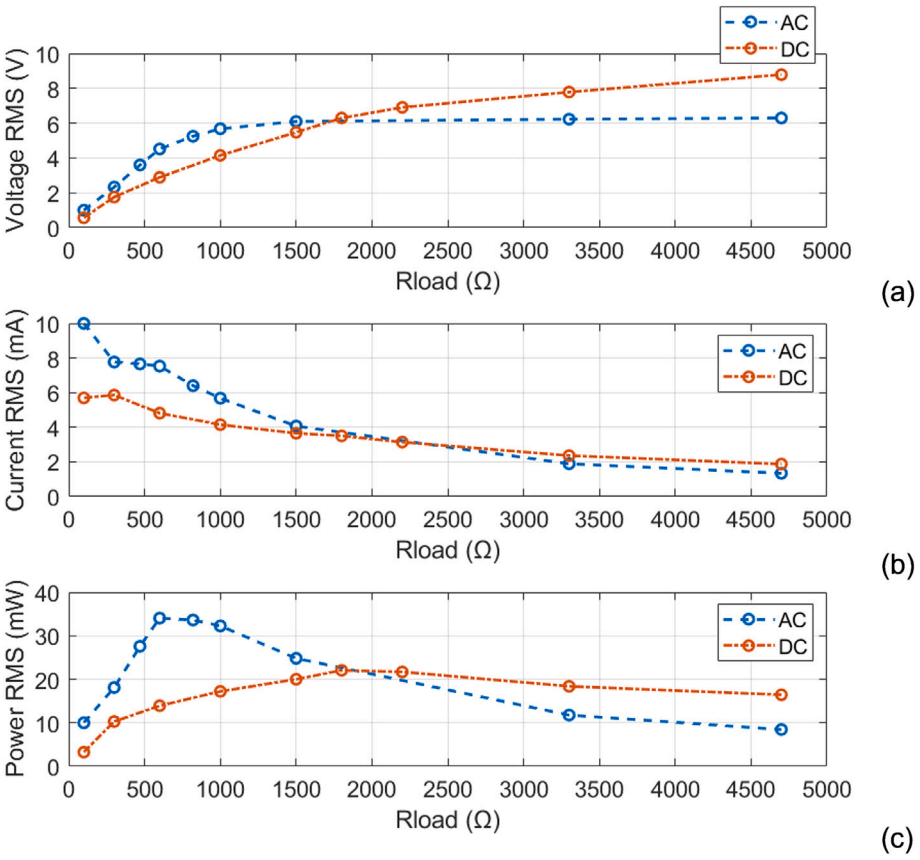

Fig. 5. AC/DC load tests comparison with excitation amplitude 0.4 g at 4 Hz and SC = 1000 μF for (a) voltage, (b) current, (c) power.

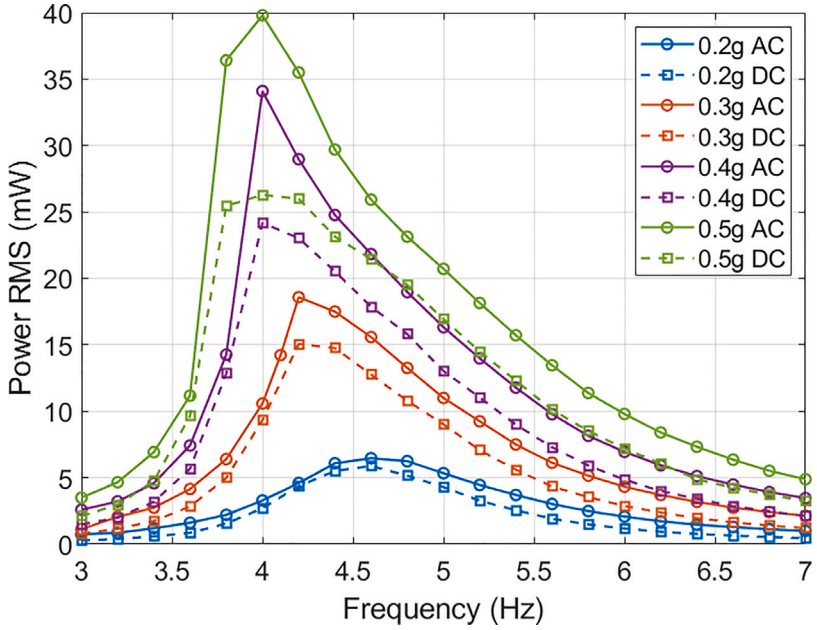

Fig. 6. AC/DC FRFs comparison with 0.2–0.5 g excitation amplitudes and frequency sweep 3–7 Hz.

WSN even when the train stops. The small capacity of the battery is chosen to better visualize the voltage charge/discharge in a reasonable amount of time. For the real working conditions, greater capacities should be used to have a stronger energy back-up. Battery charge tests are performed to quantify the input charging current considering the dependence of the GVEH generated power on the load. The input excitation is a sinusoidal signal having amplitudes from 0.2 to 0.5 g and the corresponding resonance frequency following the FRFs. The battery charge module BQ25570 consumes some of the input power to boost the input voltage to the charging level of 4.2 V. Moreover, BQ25570 also activates the buck–boost DC–DC converter to set the load output voltage at 3.3 V. Hence, the storage module efficiency should be evaluated and aggregated with the rectification efficiency to estimate the net charging power. The charge tests start at cut-off

Table 1
Battery charge experimental tests results.

Excitation	$V_{DC,in}$ (V)	$I_{DC,in}$ (mA)	$P_{DC,in}$ (mW)	V_{bat} (V)	I_{bat} (mA)	P_{bat} (mW)	η_{bat}	PCE
0.2 g @ 4.5 Hz	1.50	2.08	3.12	3.40	0.75	2.49	80%	52%
0.3 g @ 4.3 Hz	2.34	3.30	7.71	3.60	1.87	6.73	87%	57%
0.4 g @ 4.1 Hz	2.83	4.19	11.85	3.60	2.89	10.4	88%	57%
0.5 g @ 4.1 Hz	3.23	5.28	17.05	3.60	4.09	14.7	86%	56%

discharge voltage of 2.8 V, last one hour and are not complete to the full charge voltage of 4.2 V. This is due to the small charging currents and the consequent unreasonable long test durations. The crucial information resulting from these tests is the net charging power that must be compared to the load power consumption for a duty cycle definition. The battery charge level reaches the nominal voltage after one hour with excitation amplitudes from 0.3 g above, while a longer period is necessary with lower excitations. Table 1 reports the mean DC input voltage ($V_{DC,in}$), current ($I_{DC,in}$), power ($P_{DC,in}$) after the ADRC and SC entering the BCM-BBDC and the effective output charging voltage (V_{bat}), current (I_{bat}), power (P_{bat}) to the battery after the BCM-BBDC to evaluate the storage efficiency (η_{bat}) under different resonance conditions from 0.2 g to 0.5 g excitation amplitudes following the FRF curves in Fig. 6.

$$\eta_{bat} = \frac{P_{bat}}{P_{DC,in}} \tag{5}$$

The storage efficiency is above 80% for all excitation conditions, with better results for higher amplitudes. Finally, it is possible to compute the total power conversion efficiency of the circuit (PCE) as the ratio between battery charging power and AC input power in resonance conditions.

$$PCE = \frac{P_{bat}}{P_{AC}} = \eta_{Prect,int} * \eta_{bat} \tag{6}$$

The equivalent circuit resistive value can be derived from Table 1 since the DC generated power is about 12 mW at 0.4 g 4.1 Hz sinusoidal input. Load tests at this specific excitation amplitude and frequency in Fig. 5 show that 12 mW power is generated with a resistive load of about 600 Ω, being the optimum value in AC without the reactive component. As a result, the introduction of the smoothing capacitor and consequent optimum load shifting to 1800 Ω worsens the conversion efficiency. However, the smoothing capacitor of the chosen size of 1000 μF is still mandatory to have $\eta_{Vripple}$ lower than 10%, thus guaranteeing a stable DC input to the BQ25570 PMIC on the harvesting side.

Master–slave communication tests and duty cycle evaluation

The last section of the EH-WSN design process is the evaluation of the load power draw. As described in Section "Wireless sensor node description", the harvested energy supplies power to the MCU, SU and CU at 3.3 V from the BBDC output port. The MCU draws about 4 mA in active mode and 60 μA in sleep phase. During the active mode, the MCU reads the temperature data from SU and sends the value to a master node through the CU. The SU has a current draw of 200 μA in active mode and 0.1 μA in sleep mode. The most conspicuous contribution to the node power consumption is related to the RX and TX operations. The extent of drawn energy depends on power of the RF signal emitted by the antenna (decibel per milliwatts dBm). The higher the dBm, the higher the strength of the signal and the quality of communication, at the cost of a higher power consumption [67]. The CU has the possibility to set the output signal power (SP) from 14 dBm to 20 dBm. A digital oscilloscope (TDS210, Tektronix Inc., Oregon) is used for an in-depth analysis of WSN power consumption during the activity phases for different signal power outputs. Supplementary material shows that the WSN activity phase can be subdivided into steps having different current draws. First, the node wakes up from deep sleep and enters the listening phase, waiting for the reception of a packet, consuming about 20 mA. Subsequently, the WSN enters the RX-TX phase corresponding to the two current peaks respectively. Finally, after the data post-processing the WSN enters deep sleep phase again waiting for the next wake-up. The overall activity phase duration is about 12 ms and the mean current draw depends on the CU signal power, increasing almost linearly from 20 mA at 14 dBm to 28 mA at 20 dBm.

Experimental master–slave communication tests are performed at different gain power and relative distance between the two nodes for power consumption, received signal strength indicator (RSSI) and packet loss rate (PLR) evaluation. RSSI and PLR are used as performance metrics to determine the CU transmission quality. RSSI is measured in dBm and is an indicator of the power detected at the antenna port. PLR is the ratio between the unsuccessful and successful packet transmission and should not exceed the value of 10% for undesired communication errors between master and slave nodes [63]. Both master and slave nodes are equipped with a wire antenna 8.2 cm long to match the Europe standard communication frequency of 868 MHz. The RSSI/PLR communication tests are performed inside a closed footbridge having metallic structure to simulate the working conditions on a train. The slave node is the WSN (MCU, CU, SU) directly powered by the battery. The master node receives and prints the live datastream from the slave node placed at increasing relative distance. For each position the slave node sends 200 packet data and waits for an acknowledgment feedback of correct communication from the master. The tests are repeated for different SPs of the CUs ranging from 14 to 20 dBm. The chosen relative distances for the tests are 20 and 40 m to simulate communication along one or two wagons. Table Supplementary material reports the master–slave communication tests results in terms of mean RSSI for 20 and 40 m range ($RSSI_{m,20}$ and $RSSI_{m,40}$) and PLR ($PLR_{m,20}$ and $PLR_{m,40}$) for SPs of 14, 16, 18 and 20 dBm. The influence of both SP and relative distance on the RSSI and PLR is weak, resulting in an overall constant performance of the CU. PLR is zero in all conditions except from the case of 14 dBm and 40 m range where it is only 1%, thus being negligible.

The communication tests results need to be cross-referenced with the power consumption analysis of the CU at different SPs. Considering that the communication tests demonstrate an adequate transmission quality already for the lowest output power of 14 dBm, this setting is chosen for the WSN working conditions to minimize power consumption. The load draws a mean current of 20 mA at 3.3 V resulting in 66 mW of power during activity period of 12 ms. The power consumption and battery charge tests lead to the definition of the duty cycle as the number of activity phases in a certain time frame. Considering the battery charging power under the different excitation conditions, the duty cycle is defined so that the net battery charge level does not decrease to guarantee ideally infinite lasting performance of the WSN. Fig. 7 reports the WSN mean power consumption (P_{WSN}) for different duty cycles ranging from 1 activity over 0.1 to 60 s of sleep period, compared with the input charging power under GVEH resonance conditions (P_{bat} in Table 1). For duty cycles of one activity over periods of sleep phases longer than one second, P_{bat} exceeds P_{WSN} for resonance conditions under excitations greater than 0.2 g. This because the WSN sleeps for 99% of considered time frame consuming only 0.2 mW. More specifically, the duty cycle could be reduced up to about 0.5 s with the lowest excitation amplitude of 0.2 g at resonance frequency. Further duty cycle reductions up to one activity every 0.1 s require the excitation amplitudes to be at least 0.4 g for a net positive battery charge power. Considering the destined application of

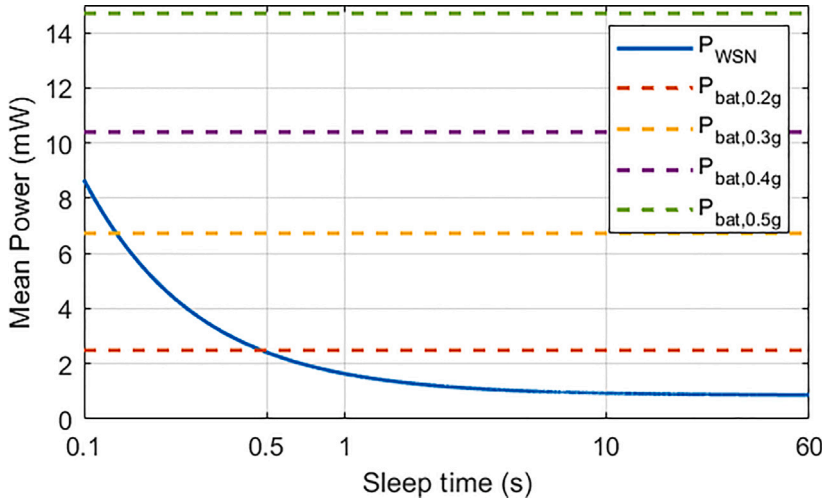

Fig. 7. Comparison between WSN mean power consumption for different duty cycles and mean charging power at different excitation amplitudes.

temperature monitoring, a sampling frequency of 1 Hz is common as the temperature transient is relatively slow due to braking time lasting several seconds and relatively low travel speeds of freight trains [68–70]. As a result, the GVEH-WSN design is experimentally validated to guarantee long-lasting and reliable performance even under low excitation amplitudes.

Conclusions

A gravitational vibration-based electromagnetic energy harvester powering a WSN for freight trains monitoring applications is presented. The GVEH configuration, main characteristics and features resulting from an optimization design process are described. The main focus of this research is the rectification circuit and battery management components optimization in relation to the GVEH output power Frequency Response Functions. Experimental tests are performed to evaluate the most efficient passive full-wave rectification circuit for AC ultra-low power generated by the GVEH. Negative voltage converter configuration, involving the use of two P-FETs, two N-FETs and a schottky diode to block reverse currents, has shown the best performance with a smoothing capacitor of 1000 μF, achieving a power rectification efficiency of 65% for 0.2–0.5 g excitation amplitudes in the frequency range of 3–10 Hz. The smoothing capacitor size results from a trade-off between the dampening of the mean power peak in the FRFs and the reduction of the voltage ripple potentially harmful to the circuit. Experimental load tests show that the resistive load maximizing GVEH output power shifts from 600 Ω in AC to 1800 Ω in DC with the smoothing capacitor. This phenomenon results in a mismatch between the PMIC equivalent resistive load and the optimum power extraction, worsening the conversion efficiency. Further analysis for a better impedance match should be performed since the smoothing capacitor is mandatory for voltage ripple reduction of the feeding DC stable input to the BQ25570. Afterwards, the battery management circuit efficiency is tested during charge with active DC–DC buck–boost converter to have fixed output voltage at 3.3 V for the load. The WSN power consumption is experimentally evaluated during sleep and active phases with different RF signal output power. The choice of 14 dBm output power minimizes power consumption but guarantees adequate transmission quality in a metallic structure resembling the freight train working conditions. Finally, the WSN duty cycle influence on the average power consumption is experimentally tested. An activity phase of one data collection and transmission every second or more requires less power than the generated amount of the GVEH in resonance conditions for excitation amplitudes of 0.2 g and above, resulting in a net positive input charge to the battery. The power management circuit and components design process is experimentally validated to guarantee long-lasting and reliable performance of the device under laboratory resonance conditions. Future works will involve the experimental in-field tests of the GVEH to evaluate the input charge under real freight train vibrations during working conditions. The duty cycle will be optimized considering real extracted power on the train, exploring the possibility of an adaptive solution for the specific monitored variables and the train activity during the day.

CRediT authorship contribution statement

Mirco Lo Monaco: Writing – review & editing, Writing – original draft, Visualization, Validation, Software, Methodology, Investigation, Formal analysis, Data curation, Conceptualization. **Caterina Russo:** Visualization, Validation, Software, Methodology, Investigation, Formal analysis, Data curation, Conceptualization. **Aurelio Somà:** Validation, Supervision, Resources, Project administration, Methodology, Funding acquisition, Conceptualization.

Declaration of competing interest

The authors declare that they have no known competing financial interests or personal relationships that could have appeared to influence the work reported in this paper.

Data availability

Data will be made available on request.

Supplementary data

Supplementary material related to this article can be found online at https://doi.org/10.1016/j.seta.2024.103964.

References

[1] Shirvanimoghaddam M, Shirvanimoghaddam K, Abolhasani MM, Farhangi M, Zahiri Barsari V, Liu H, et al. Towards a green and self-powered Internet of Things using piezoelectric energy harvesting. IEEE Access 2019;7:94533–56. http://dx.doi.org/10.1109/ACCESS.2019.2928523.

[2] Vailshery LS. Number of IoT connected devices worldwide 2019–2023, with forecasts to 2030. 2023, URL https://www.statista.com/statistics/1183457/iot-connected-devices-worldwide/. [Accessed: 03 May 2024].

[3] Singh J, Kaur R, Singh D. Energy harvesting in wireless sensor networks: A taxonomic survey. Int J Energy Res 2021;45:118–40. http://dx.doi.org/10.1002/er.5816.

[4] Hao D, Kong L, Zhang Z, Kong W, Tairab AM, Luo X, et al. An electromagnetic energy harvester with a half-wave rectification mechanism for military personnel. Sustain Energy Technol Assess 2023;57:103184. http://dx.doi.org/10.1016/j.seta.2023.103184.

[5] Wang S. Sports training monitoring of energy-saving IoT wearable devices based on energy harvesting. Sustain Energy Technol Assess 2021;45:101168. http://dx.doi.org/10.1016/j.seta.2021.101168.

[6] Cappelli I, Fort A, Pozzebon A, Tani M, Trivellin N, Vignoli V, et al. Autonomous IoT monitoring matching spectral artificial light manipulation for horticulture. Sensors 2022;22. http://dx.doi.org/10.3390/s22114046.

[7] Ahmad FF, Ghenai C, Bettayeb M. Maximum power point tracking and photovoltaic energy harvesting for Internet of Things: A comprehensive review. Sustain Energy Technol Assess 2021;47:101430. http://dx.doi.org/10.1016/j.seta.2021.101430.

[8] Paolini G, Guermandi M, Masotti D, Shanawani M, Benassi F, Benini L, et al. RF-powered low-energy sensor nodes for predictive maintenance in electromagnetically harsh industrial environments. Sensors (Switzerland) 2021;21:1–18. http://dx.doi.org/10.3390/s21020386.

[9] Shi Y, Wang Y, Deng Y, Gao H, Lin Z, Zhu W, et al. A novel self-powered wireless temperature sensor based on thermoelectric generators. Energy Convers Manage 2014;80:110–6. http://dx.doi.org/10.1016/j.enconman.2014.01.010.

[10] Tan X, Fang Z, Pan Y, Zhang Z, Wu X, Wang J, et al. A self-adapting wind energy harvesting system for application in canyon bridge. Sustain Energy Technol Assess 2022;54:102878. http://dx.doi.org/10.1016/j.seta.2022.102878.

[11] Velusamy VR, Foong FM, Nik Mohd NAR, Thein CK. Bistable dual cantilever flutter for potential wind energy harvesting applications. Sustain Energy Technol Assess 2024;63:103637. http://dx.doi.org/10.1016/j.seta.2024.103637.

[12] Song C, Zhu X, Wang M, Yang P, Chen L, Hong L, et al. Recent advances in ocean energy harvesting based on triboelectric nanogenerators. Sustain Energy Technol Assess 2022;53:102767. http://dx.doi.org/10.1016/j.seta.2022.102767.

[13] Barua A, Salauddin Rasel M. Advances and challenges in ocean wave energy harvesting. Sustain Energy Technol Assess 2024;61:103599. http://dx.doi.org/10.1016/j.seta.2023.103599.

[14] Singh P, Elmi Z, Meriga VK, Pasha J, Dulebenets MA. Internet of Things for sustainable railway transportation: Past, present, and future. Clean Logist Supply Chain 2022;4. http://dx.doi.org/10.1016/j.clscn.2022.100065.

[15] Santa J, Bernal-Escobedo L, Sanchez-Iborra R. On-board unit to connect personal mobility vehicles to the IoT. In: The 17th international conference on mobile systems and pervasive computing, vol. 175, Elsevier B.V.; 2020, p. 173–80. http://dx.doi.org/10.1016/j.procs.2020.07.027.

[16] Rodriguez JC, Nico V, Punch J. Powering wireless sensor nodes for industrial IoT applications using vibration energy harvesting. In: 2019 IEEE 5th world forum on Internet of Things. 2019, p. 392–7. http://dx.doi.org/10.1109/WF-IoT.2019.8767352.

[17] Somà A, Pasquale GD. Device for diagnosing railway bogies by applying an energy-autonomous measuring and transmitting bolt, and corresponding control method. 2011, WIPO Patent, WO2011117718A1.

[18] Somà A, Fraccarollo F, Pasquale GD. Magneto-inductive energy harvester device, having an internal guide magnetic suspension. 2013, EU Patent, EP2862264.

[19] Pasquale GD, Somà A, Fraccarollo F. Piezoelectric energy harvesting for autonomous sensors network on safety-improved railway vehicles. Proc Inst Mech Eng C 2012;226:1107–17. http://dx.doi.org/10.1177/0954406211418158.

[20] Zhang Q, Liu Z, Jiang X, Peng Y, Zhu C, Li Z. Experimental investigation on performance improvement of cantilever piezoelectric energy harvesters via escapement mechanism from extremely low-frequency excitations. Sustain Energy Technol Assess 2022;53:102591. http://dx.doi.org/10.1016/j.seta.2022.102591.

[21] Li Y, Li J, Liu Z, Hu H, Hu J, Wang J, et al. Theoretical and experimental investigation of magnet and coil arrays optimization for power density improvement in electromagnetic vibration energy harvesters. Energy Convers Manage 2023;293. http://dx.doi.org/10.1016/j.enconman.2023.117411.

[22] Wang K, Liu W, Tang Y, Pei J, Kang S, Wu Z. Widening the bandwidth of vibration energy harvester by automatically tracking the resonant frequency with magnetic sliders. Sustain Energy Technol Assess 2023;58:103368. http://dx.doi.org/10.1016/j.seta.2023.103368.

[23] Dai X, Wang H, Wu H, Pan Y, Luo D, Ahmed A, et al. A hybrid energy harvesting system for self-powered applications in shared bicycles. Sustain Energy Technol Assess 2022;51:101891. http://dx.doi.org/10.1016/j.seta.2021.101891.

[24] Li J, Cheng L, Wan N, Ma J, Hu Y, Wen J. Hybrid harvesting of wind and wave energy based on triboelectric-piezoelectric nanogenerators. Sustain Energy Technol Assess 2023;60:103466. http://dx.doi.org/10.1016/j.seta.2023.103466.

[25] Shaukat H, Ali A, Ali S, Altabey WA, Noori M, Kouritem SA. Applications of sustainable hybrid energy harvesting: A review. J Low Power Electron Appl 2023;13. http://dx.doi.org/10.3390/jlpea13040062.

[26] Izhar, Iqbal M, Khan F. Hybrid acoustic, vibration, and wind energy harvester using piezoelectric transduction for self-powered wireless sensor node applications. Energy Convers Manage 2023;277. http://dx.doi.org/10.1016/j.enconman.2022.116635.

[27] Salim M, Dayou J, Aljibori HS, Salim D, Shebeeb A. A low frequency hybrid harvester with ring magnets. Sustain Energy Technol Assess 2016;13:23–30. http://dx.doi.org/10.1016/j.seta.2015.11.006.

[28] Beeby SP, Torah RN, Tudor MJ, Glynne-Jones P, O'Donnell T, Saha CR, et al. A micro electromagnetic generator for vibration energy harvesting. J Micromech Microeng 2007;17:1257–65. http://dx.doi.org/10.1088/0960-1317/17/7/007.

[29] Gonzalo AP, Entezami M, Weston P, Roberts C, Marquez FPG. Railway track and vehicle onboard monitoring: A review. In: International conference on management science and engineering management, vol. 409, EDP Sciences; 2023, http://dx.doi.org/10.1051/e3sconf/202340902014.

[30] Bosso N, Magelli M, Zampieri N. Monitoring systems for railways freight vehicles. Int J Comput Methods Exp Measur 2022;10:359–71. http://dx.doi.org/10.2495/CMEM-V10-N4-359-371.

[31] Lazarescu MT, Poolad P. Asynchronous resilient wireless sensor network for train integrity monitoring. IEEE Internet Things J 2021;8:3939–54. http://dx.doi.org/10.1109/JIOT.2020.3026243.

[32] Zhao Y, Yu X, Chen M, Zhang M, Chen Y, Niu X, et al. Continuous monitoring of train parameters using IoT sensor and edge computing. IEEE Sens J 2021;21:15458–68. http://dx.doi.org/10.1109/JSEN.2020.3026643.

[33] Bernal E, Spiryagin M, Cole C. Onboard condition monitoring sensors, systems and techniques for freight railway vehicles: A review. IEEE Sens J 2019;19:4–24. http://dx.doi.org/10.1109/JSEN.2018.2875160.

[34] Bosso N, Magelli M, Zampieri N. Application of low-power energy harvesting solutions in the railway field: A review. Veh Syst Dyn 2021;59:841–71. http://dx.doi.org/10.1080/00423114.2020.1726973.

[35] Pasquale GD, Somà A, Zampieri N. Design, simulation, and testing of energy harvesters with magnetic suspensions for the generation of electricity from freight train vibrations. J Comput Nonlinear Dynam 2012;7. http://dx.doi.org/10.1115/1.4006920.

[36] Wu X, Zhang T, Liu J, Zhang T, Kong W, Pan Y, et al. A vibration energy harvesting system for self-powered applications in heavy railways. Sustain Energy Technol Assess 2022;53:102373. http://dx.doi.org/10.1016/j.seta.2022.102373.

[37] Liu M, Zhang Y, Fu H, Qin Y, Ding A, Yeatman EM. A seesaw-inspired bistable energy harvester with adjustable potential wells for self-powered internet of train monitoring. Appl Energy 2023;337. http://dx.doi.org/10.1016/j.apenergy.2023.120908.

[38] Gao M, Cong J, Xiao J, He Q, Li S, Wang Y, et al. Dynamic modeling and experimental investigation of self-powered sensor nodes for freight rail transport. Appl Energy 2020;257. http://dx.doi.org/10.1016/j.apenergy.2019.113969.

[39] Sun Q, Patil S, Stoute S, Sun NX, Lehman B. Optimum design of magnetic inductive energy harvester and its AC-DC converter. In: 2012 IEEE energy conversion congress and exposition. 2012, p. 394–400. http://dx.doi.org/10.1109/ECCE.2012.6342795.

[40] Gomez-Casseres EA, Arbulú SM, Franco RJ, Contreras R, Martínez J. Comparison of passive rectifier circuits for energy harvesting applications. In: 2016 IEEE Canadian conference on electrical and computer engineering. 2016, p. 1–6. http://dx.doi.org/10.1109/CCECE.2016.7726840.

[41] Roy S, Azad AN, Baidya S, Khan F. A comprehensive review on rectifiers, linear regulators, and switched-mode power processing techniques for biomedical sensors and implants utilizing in-body energy harvesting and external power delivery. IEEE Trans Power Electron 2021;36:12721–45. http://dx.doi.org/10.1109/TPEL.2021.3075245.

[42] Edla M, Lim YY, Padilla RV, Deguchi M. An improved rectifier circuit for piezoelectric energy harvesting from human motion. Appl Sci (Switzerland) 2021;11:1–23. http://dx.doi.org/10.3390/app11052008.

[43] Fang LH, Rahim RA, Fahmi MI, Nordin JM, Zain ASM. Review of active circuit and passive circuit techniques to improve the performance of highly efficient energy harvesting systems. J Adv Res Appl Sci Eng Technol 2023;31:271–90. http://dx.doi.org/10.37934/ARASET.31.1.271290.

[44] Xu Y, Bader S, Magno M, Mayer P, Oelmann B. System implementation trade-offs for low-speed rotational variable reluctance energy harvesters. Sensors 2021;21. http://dx.doi.org/10.3390/s21186317.

[45] Belal E, Mostafa H, Said MS. Comparison between active AC-DC converters for low power energy harvesting systems. In: 2015 27th international conference on microelectronics. 2015, p. 253–6. http://dx.doi.org/10.1109/ICM.2015.7438036.

[46] Arul ACA, Samuel ER. Efficiency evaluation of a MOSFET bridge rectifier for powering LEDs using piezo-electric energy harvesting systems. Automatika – J Control Measur Electron Comput Commun 2016;57. http://dx.doi.org/10.7305/automatika.2016.10.959.

[47] Srinivasan R, Mangalanathan U, Gandhi U, Karlmarx LR. Bridgeless active rectifier for piezoelectric energy harvesting. IET Circuits Dev Syst 2019;13:1078–85. http://dx.doi.org/10.1049/iet-cds.2018.5576.

[48] Russo C, Lo Monaco M, Somà A. Energy harvester duty cycle evaluation for railway vehicle health monitoring. IOP Conf Ser: Mater Sci Eng 2022;1214:012046. http://dx.doi.org/10.1088/1757-899x/1214/1/012046.

[49] Lo Monaco M, Russo C, Somà A. Investigation of gravitational energy harvesters for IoT power supply in freight train monitoring. In: 2023 25th European conference on power electronics and applications. 2023, p. P.1–8. http://dx.doi.org/10.23919/EPE23ECCEEurope58414.2023.10264497.

[50] Li Y, Li J, Liu Z, Hu H, Hu J, Wang J, et al. Theoretical and experimental investigation of magnet and coil arrays optimization for power density improvement in electromagnetic vibration energy harvesters. Energy Convers Manage 2023;293. http://dx.doi.org/10.1016/j.enconman.2023.117411.

[51] Ordoñez V, Arcos R, Romeu J. A high-performance electromagnetic vibration energy harvester based on ring magnets with Halbach configuration. Energy Convers Manag: X 2022;16. http://dx.doi.org/10.1016/j.ecmx.2022.100280.
[52] Nicolini L, Castagnetti D. A wideband low frequency 3D printed electromagnetic energy harvester based on orthoplanar springs. Energy Convers Manage 2024;300. http://dx.doi.org/10.1016/j.enconman.2023.117903.
[53] Lo Monaco M, Russo C, Somà A. Identification procedure for design optimization of gravitational electromagnetic energy harvesters. Appl Sci 2023;13(4). http://dx.doi.org/10.3390/app13042736.
[54] Lo Monaco M, Russo C, Somà A. Numerical and experimental performance study of two-degrees-of-freedom electromagnetic energy harvesters. Energy Convers Manag: X 2023;18:100348. http://dx.doi.org/10.1016/j.ecmx.2023.100348.
[55] Russo C, Lo Monaco M, Fraccarollo F, Somà A. Experimental and numerical characterization of a gravitational electromagnetic energy harvester. Energies 2021;14(15). http://dx.doi.org/10.3390/en14154622.
[56] Carneiro P, Soares Dos Santos M, Rodrigues A, JAF F, Simoes J, Marques A, et al. Electromagnetic energy harvesting using magnetic levitation architectures: A review. Appl Energy 2020;260:114191. http://dx.doi.org/10.1016/j.apenergy.2019.114191.
[57] Royo-Silvestre I, Beato-López JJ, Gómez-Polo C. Optimization procedure of low frequency vibration energy harvester based on magnetic levitation. Appl Energy 2024;360. http://dx.doi.org/10.1016/j.apenergy.2024.122778.
[58] Bijak J, Trawiński T, Szczygieł M, Kowalik Z. Modelling and investigation of energy harvesting system utilizing magnetically levitated permanent magnet. Sensors 2022;22. http://dx.doi.org/10.3390/s22176384.
[59] Ibrahim MA, Hassan G, Hassanein HS, Obaia K. A wireless sensor platform for industrial non-hermetic metallic enclosures. In: 2017 13th international wireless communications and mobile computing conference. Institute of Electrical and Electronics Engineers Inc.; 2017, p. 165–70. http://dx.doi.org/10.1109/IWCMC.2017.7986280.
[60] Texas instruments, bq25570 nano power boost charger and buck converter for energy harvester powered applications. 2019, BQ25570, Texas Instruments, URL https://www.ti.com/lit/ds/symlink/bq25570.pdf. Rev. G, [Accessed: 03 May 2024].
[61] Microchip, MCP9808 0.5C maximum accuracy digital temperature sensor. 2011, MCP9808, Microchip, URL https://ww1.microchip.com/downloads/en/DeviceDoc/25095A.pdf. [Accessed: 03 May 2024].
[62] Hoperf electronic, RFM69HCW ISM transceiver module v1.1. 2006, RFM69HCW, Hoperf Electronic, URL https://www.hoperf.com/modules/rf_transceiver/RFM69HCW.html. [Accessed: 03 May 2024].
[63] Yang Z, Ghubaish A, Unal D, Jain R. Factors affecting the performance of sub-1 GHz IoT wireless networks. Wirel Commun Mob Comput 2021;2021. http://dx.doi.org/10.1155/2021/8870222.
[64] Yilmaz M, Tunkar BA, Park S, Elrayes K, Mahmoud MA, Abdel-Rahman E, et al. High-efficiency passive full wave rectification for electromagnetic harvesters. J Appl Phys 2014;116. http://dx.doi.org/10.1063/1.4896668.
[65] Li X, Rogers ES, Nabavi S, Zhang L. Effect of varying threshold voltage on efficiency of CMOS rectifiers for piezoelectric energy harvesting applications. In: Canadian conference on electrical and computer engineering, vol. 2020-August, Institute of Electrical and Electronics Engineers Inc.; 2020, http://dx.doi.org/10.1109/CCECE47787.2020.9255679.
[66] Balguvhar S, Bhalla S. Assessment of mosfet/diode based rectifier interface circuits for piezoelectric energy harvesting from structural vibrations. Analog Integr Circuits Signal Process 2023;115:169–82. http://dx.doi.org/10.1007/s10470-023-02143-1.
[67] Chandu K, Gorrepotu R, Swaroop KN, Dasari M. Performance analysis of sub-GHz system for IoT applications. Int J Electr Electron Eng Telecommun 2021;10:125–32. http://dx.doi.org/10.18178/ijeetc.10.2.125-132.
[68] Aimar M. Study of an onboard wired-wireless health monitoring system equipped with power save algorithm for freight railway wagons [Ph.D. thesis], Politecnico di Torino; 2018, http://dx.doi.org/10.6092/polito/porto/2706128.
[69] Choi DB, Jeong R-G, Kim Y, Chai J. Comparisons between braking experiments and longitudinal train dynamics using friction coefficient and braking pressure modeling in a freight train. Open Transport J 2020;14:154–63. http://dx.doi.org/10.2174/1874447802014010154.
[70] Zhang Y, Liu Z, Stichel S. Study on the braking distance of composite brake blocks covered with ice for freight trains in winter. Proc Inst Mech Eng F 2023;237:1050–9. http://dx.doi.org/10.1177/09544097231151474.